Frequency and Temperature-Dependent Power Cable Modelling for Stability Analysis of Grid-Connected Inverter

Zhou, Weihua; Wang, Yanbo; Chen, Zhe

Published in:
Proceedings of 2018 IEEE 4th Southern Power Electronics Conference (SPEC)

DOI (link to publication from Publisher):
10.1109/SPEC.2018.8635852

Publication date:
2018

Document Version
Accepted author manuscript, peer reviewed version

Frequency and Temperature-Dependent Power Cable Modelling for Stability Analysis of Grid-Connected Inverter

Weihua Zhou*, Yanbo Wang†, and Zhe Chen‡
Department of Energy Technology
Aalborg University
Aalborg, Denmark
*wez@et.aau.dk, †ywa@et.aau.dk, ‡zch@et.aau.dk

***Abstract*—This paper presents a RLC circuit model of long transmission cable (LTC) with consideration of frequency and temperature-dependent characteristics. Per-unit-length (p.u.l.) impedance of the LTC considering frequency-dependent characteristics are first calculated and fitted by Vector Fitting (VF) algorithm. Then, the fitted model of the p.u.l. impedance is represented by a Π section, which consists of a series of RL branches and two parallel capacitors. Impedance model of LTC with arbitrary length can be established by cascading several Π sections. In addition, the effect of ambient temperature variation on electrical performance of LTC are investigated. Simulation results show that the proposed RLC circuit model is able to reveal practical frequency and temperature characteristics, which may be used to investigate effect of power cable on stability of grid-connected inverter.**

***Index Terms*—Frequency-dependent, grid-connected inverter, long transmission cable, RLC equivalent circuit, temperature-dependent.**

I. Introduction

Offshore wind power generation has been paid increasing attentions in recent years [1], [2]. Compared with onshore wind power plant, offshore wind farms are commonly integrated into power grid by offshore substation and long transmission cable (LTC) due to remote transmission distances [1]. Voltage source converters (VSCs) have been widely applied in offshore wind power plant [2]–[4].

However, oscillation phenomena have been frequently reported in offshore wind power plants with LTC, where harmonic-frequency resonance may be triggered at multiple frequencies due to distributed parasitic capacitance of LTC [5]. It's urgent to find out the effect of LTC on resonance phenomena of grid-connected inverter (GCI) system.

Previous work about modelling of power cable has been presented in [6]–[9]. LTC is commonly modelled as a simple inductor, which fails to reveal practical frequency characteristics and perform inaccurate stability assessment [6]. Furthermore, frequency-dependent circuit models of LTC considering distributed parasitic capacitance are established in [7]–[9], in which multiple cascaded-Π section circuit model is used. However, resistance and inductance of per-unit-length (p.u.l.) LTC are modelled as a fixed resistor and inductor, which cannot reveal the practical frequency-dependent characteristics and corresponding damping characteristics. To simulate practical frequency characteristics of LTC, extra RL branches are introduced, which are paralleled with each Π section [10], [11]. The number of parallel RL branches and cascaded Π sections can be optimized based on the length of LTC.

In addition, electrical characteristic of LTC may be affected due to ambient temperature variation. Severe temperature fluctuation can be up to 20 °C under severe weather conditions [12]. The temperature variation may cause electrical parameters perturbation along LTC [13], which thus influences terminal impedance characteristics. In [14], the consequences of 20% increased uncorrected line resistance caused by ambient temperature are shown. However, temperature-dependent characteristics have been paid limited attentions in existing frequency-dependent models. The effect of cable resistance perturbation caused by temperature fluctuation on high frequency resonance phenomena of DFIG system has been studied in [9]. However, temperature-dependent LTC model is not established. A temperature-dependent LTC model considering longitude temperature variation is established in [13]–[16]. However, the established temperature-dependent LTC model merely focuses on state estimation, e.g. line power transmission capability [13], [16], which was not applied to stability analysis. Therefore, this paper develops a RLC circuit model of LTC with consideration of frequency and temperature-dependent characteristics, which may be used to investigate effect of cable electrical characteristics on stability of GCI.

The main contributions of this paper can be briefly explained as follows. (1) Frequency and temperature-dependent characteristics of LTC is established in RLC circuit model, where

This work was supported by the ForskEL and EUDP Project "Voltage Control and Protection for a Grid towards 100% Power Electronics and Cable Network (COPE)" (Project No.: 880063).

978-1-5386-8257-9/18/$31.00 © 2018 European Union

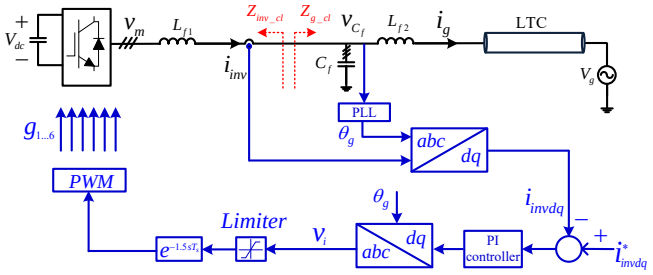

Fig. 1. The studied three-phase GCI-LTC system diagram.

the effect of temperature variation on electrical parameters perturbation is simulated by correcting electrical parameters of each Π section. (2) The impact of LTC length variation on stability of GCI is investigated.

II. Impedance Modelling of GCI

Fig. 1 shows diagram of GCI with LTC, which consists of LCL filter, current controller in dq frame, synchronous reference frame phase-locked loop (SRF-PLL) and modulator. The inverter side current feedback is used, since the current is the superposition of the grid side and filter capacitor currents (Capacitor current feedback can provide damping effect) [17], [18]. The grid is emulated as an ideal voltage source V_g, and LTC is used to connect the GCI and grid.

Small signal stability of GCI can be identified by means of impedance-based stability criterion, which plots the Nyquist diagram of the minor loop gain (MLG) $T(s)$ and counts the number of encirclements [6], shown as follows,

$$T(s) = \frac{Z_{g\_cl}(s)}{Z_{inv\_cl}(s)} \tag{1}$$

where $Z_{inv\_cl}(s)$ is GCI impedance, and $Z_{g\_cl}(s)$ is equivalent grid impedance which includes C_f, L_{f2} and LTC, as shown in Fig. 1.

The GCI part in Fig. 1 can be transferred into Fig. 2, and the Norton equivalent circuit in red dotted box of Fig. 3 can be established on the basis of Fig. 2. The parameters of the Norton equivalent circuit are as follows,

$$\begin{aligned} G_{cl} &= \frac{i_{inv}}{i^*_{inv}} = \frac{G_{idq}G_dY_{L_{f1}}}{1+G_{idq}G_dY_{L_{f1}}} \\ Z_{inv\_cl} &= \frac{-v_{C_f}}{i_{inv}} = \frac{1+G_{idq}G_dY_{L_{f1}}}{Y_{L_{f1}}} \end{aligned} \tag{2}$$

where G_{idq} is the transfer function of the PI controller, G_d is digital delay which includes one sampling computational delay and 0.5 sampling modulation delay [19], $Y_{L_{f1}}$ is the admittance formula of L_{f1}.

$$\begin{aligned} G_{idq}(s) &= K_p + \frac{K_i}{s} \\ G_d(s) &= e^{-1.5sT_s} \\ Y_{Lf1}(s) &= \frac{1}{sL_{f1}} \end{aligned} \tag{3}$$

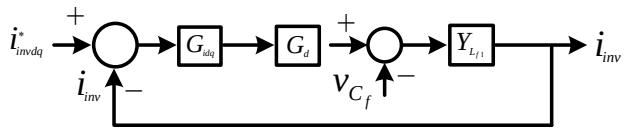

Fig. 2. Control diagram of current control loop.

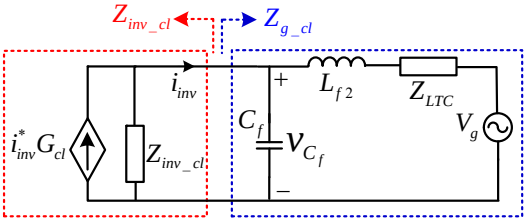

Fig. 3. Impedance model of the GCI-LTC system.

By substituting (3) into (2), Z_{inv_cl} can be represented as follows,

$$Z_{inv\_cl}(s) = sL_{f1} + (K_p + \frac{K_i}{s})e^{-1.5sT_s} \tag{4}$$

For PI controller in rotating dq frame, the impact of parameter K_i on Z_{inv_cl} in high-frequency range can be ignored. The frequency characteristics of terminal impedance of GCI can be obtained by substituting $s = jw$ into (4), shown as follows,

$$Z_{inv\_cl}(j\omega) = K_p\cos(1.5\omega T_s) + j(\omega L_{f1} - K_p\sin(1.5\omega T_s)) \tag{5}$$

It's obvious that the real part of $Z_{inv\_cl}(j\omega)$ is negative in the following frequency range, and thus the terminal impedance appears non-passive characteristics.

$$f_{NPA} = (\frac{1+4k}{6}f_s, \frac{3+4k}{6}f_s) \quad k \in N \tag{6}$$

where f_s is the sampling frequency. In practice, the frequency range below Nyquist frequency $f_s/2$ is considered ($k = 1$). Thus, the non-passivity area is $f_{NPA} = (f_s/6, f_s/2)$.

The non-passivity area is actually the potential unstable frequency range [7]. Thus, a circuit model which can reveal the practical impedance characteristics of LTC in the area should be established. However, previous works seldom take the practical frequency and temperature-dependent characteristics into account, due to the complicated modelling process. Section III will explain the practical frequency and temperature-dependent characteristics of LTC, followed by the proposed RLC circuit modelling for LTC.

III. Proposed Modelling Method for LTC

In this section, RLC circuit model of LTC with consideration of frequency and temperature-dependent characteristics is established, and detailed implementation procedure is given. The practical frequency and temperature characteristics of LTC are established in the form of RLC circuit, and then are incorporated into circuit model of power cable.

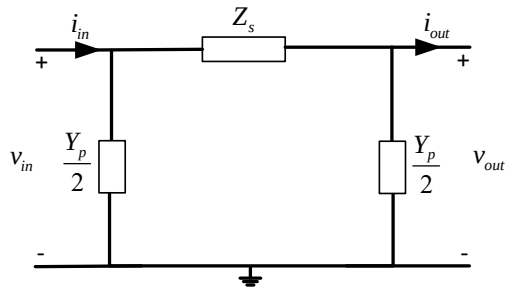

Fig. 4. Two-port network model of LTC.

A. Practical terminal impedance characteristics of LTC

1) Frequency-dependent characteristics of LTC: The terminal impedance characteristics of LTC can be reproduced by a two-port network shown in Fig. 4. The two important parameters are given as [20],

$$\begin{aligned} Z_S &= z(\omega)L\frac{\sinh(\gamma(\omega)L)}{\gamma(\omega)L} \\ Y_P &= y(\omega)L\frac{\tanh(\gamma(\omega)L/2)}{\gamma(\omega)L/2} \end{aligned} \tag{7}$$

where Z_S and Y_P are the series impedance and shunt admittance; $z(\omega)$ and $y(\omega)$ are the p.u.l. impedance and admittance. $\gamma(\omega) = \sqrt{(z(\omega)y(\omega)}$ is propagation constant, and L is the length of LTC. $z(\omega)$ and $y(\omega)$ can be represented as,

$$\begin{aligned} z(\omega) &= r(\omega) + j\omega l(\omega) \\ y(\omega) &= g(\omega) + j\omega c(\omega) \end{aligned} \tag{8}$$

where $r(\omega)$, $l(\omega)$, $g(\omega)$ and $c(\omega)$ are p.u.l. resistance, inductance, conductance and capacitance. For LTC, the values of $r(\omega)$ and $l(\omega)$ change with frequency varying. $g(\omega)$ can be ignored and $c(\omega)$ is regarded as constant [20].

2) Temperature-dependent characteristics of LTC: The p.u.l. resistance of power cable depends on the resistivity of cable conductor and the area of cross-section, which can be affected by ambient temperature. And the inductance has the similar temperature-dependent behavior [13], [15]. The temperature-dependent characteristics of p.u.l. resistance and inductance are shown as,

$$\begin{aligned} r(T_c) &= r(T_0)(1 + \alpha_r(T_c - T_0)) \\ l(T_c) &= l(T_0)(1 + \alpha_l(T_c - T_0)) \end{aligned} \tag{9}$$

where $r(T_c)$ and $l(T_c)$ are the p.u.l resistance and inductance at temperature T_c. $r(T_0)$ and $l(T_0)$ are the p.u.l resistance and inductance at temperature T_0. Besides, α_r and α_l are the temperature coefficients of resistance and reactance of power cable, which are independent on temperature and are determined by material property of power cable conductor. Here α_r and α_l are regarded as 0.00393/°C.

Fig. 5 shows the variation characteristics of p.u.l. resistance and inductance as functions of frequency and temperature. The p.u.l. resistance increases if frequency or temperature increases, and the p.u.l. inductance increases if frequency decreases or temperature increases. The p.u.l. impedance at 20 °C calculated using (8) is shown as the blue line in Fig. 6.

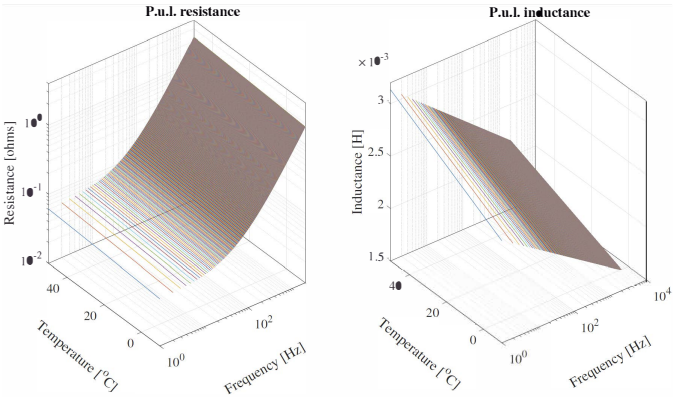

Fig. 5. The variation of p.u.l. resistance and inductance of LTC with frequency and temperature.

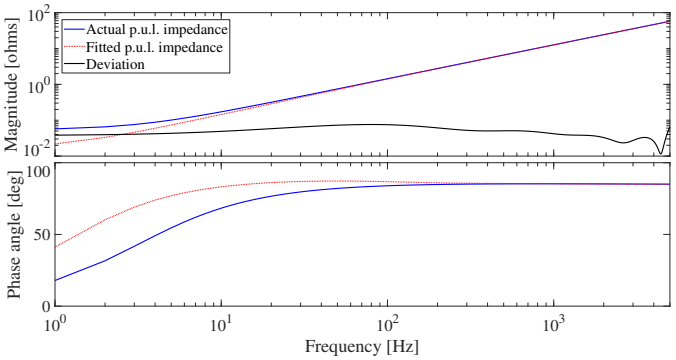

Fig. 6. P.u.l. impedance of LTC and fitted result (T=20 °C).

B. Implementation of the proposed RLC circuit modelling method

In the proposed modelling method, VF algorithm is employed to fit frequency characteristics of p.u.l. series impedance $z(\omega)$. The mathematical representation can be obtained as [21],

$$f(s) = \sum_{n=1}^{N} \frac{B_n}{s - A_n} + D + sE \tag{10}$$

where $f(s)$ is the fitted transfer function, N is the order of $f(s)$, B_n and A_n are the nth residue and pole pair. D is nonzero if the order of the numerator polynomial is not lower than the order of denominator polynomial. And E indicates the transfer function is improper [21]. In this paper, the p.u.l. impedance shown as the blue line in Fig. 6 will be fitted into form (10) using VF.

Fig. 7 shows the detailed implementation procedure of the proposed RLC circuit modelling method, which consists of three steps. Step 1 is to establish a RLC circuit model incorporating frequency-dependent characteristics. Step 2 is to derive the temperature profile along the LTC, and the

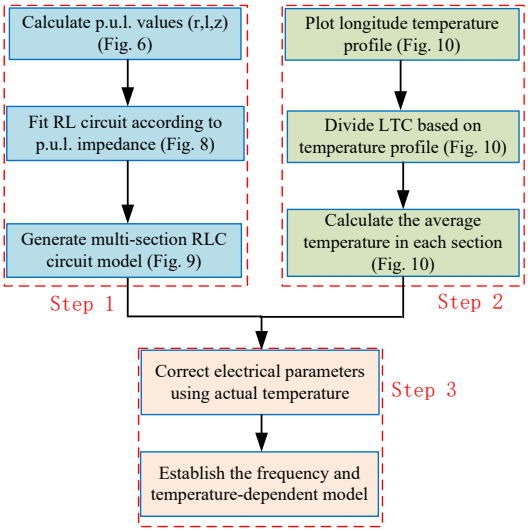

Fig. 7. Implementation procedure of the proposed RLC circuit modelling method.

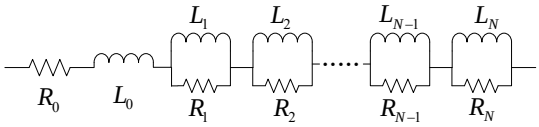

Fig. 8. RL circuit model of p.u.l. series impedance of LTC.

LTC is divided into several sections based on the temperature distribution. Finally, step 3 is to adjust the obtained RLC circuit parameters to incorporate the temperature variation information.

1) Step 1: The p.u.l. resistance, inductance and impedance at $T = 20°C$ are first calculated, shown as in Fig. 5 and Fig. 6. Then, the p.u.l. impedance is fitted by a transfer function in the form (10) using VF algorithm. In detail, when VF is implemented, the order of the transfer function increases gradually until the trade-off between accuracy and complexity is obtained. In this case, a 5-order ($N = 5$) transfer function is fitted, and its Bode diagram is plotted as the red dotted line in Fig. 6. As discussed in Section II, the potential unstable frequency range is from 1.67kHz to 5kHz if sampling frequency f_s is 10kHz. It can be seen that the fitted results accurately match practical impedance characteristics of LTC in the frequency range.

(10) is then represented by a RL network, shown as in Fig. 8. In principal, the electrical parameters of the RL circuit can be calculated from (10),

$$\begin{aligned} R_0 &= D - \sum_{i=1}^{n} \frac{B_n}{A_n}; \quad L_0 = E \\ R_k &= \frac{B_k}{A_k}; \quad L_k = -\frac{R_k}{A_k} \quad (k = 1, 2...N) \end{aligned} \tag{11}$$

Finally, multi-segment lumped-parameter RLC circuit model is adopted to represent terminal impedance characteristics of LTC, as shown in Fig. 9. The number of Π sections will be increased as extension of cable length. And the number of RL branches in each Π section will be increased if the frequency range of interest widens. The parameters of each Π section can be calculated on the basis of LTC length L, the number of Π sections m and the fitted parameters in (11), shown as follows,

$$\begin{aligned} R_0^{'} &= R_0 \frac{L}{m} \quad L_0^{'} = L_0 \frac{L}{m} \\ R_k^{'} &= R_k \frac{L}{m} \quad L_k^{'} = L_k \frac{L}{m} \\ C^{'} &= c \frac{L}{m} \quad (k = 1, 2...N) \end{aligned} \tag{12}$$

where c is the constant p.u.l. capacitance.

2) Step 2: In step 1, the longitude temperature is regarded as constant ($T = 20°C$), and the p.u.l. resistance and inductance in (8) are calculated at the fixed temperature. In step 2, the p.u.l. resistance and inductance are corrected based on temperature characteristics of LTC, shown as in Fig. 5.

The temperature-based LTC segmentation method is illustrated in Fig. 10. Temperature profile along the LTC is first measured, shown as the red line (For simplicity, linear temperature variation is considered). Then, the LTC is divided into several sections based on the measured temperature distribution, shown as $[0, x_0]$, $[x_0, x_1]$, $[x_1, x_2]$, $[x_2, x_3]$, $[x_3, L]$. For each section, the following requirement should be satisfied,

$$|T_i - T_j| < \Delta_T \tag{13}$$

where i and j are the arbitrary two points in arbitrary section, and Δ_T is the pre-defined temperature threshold value. The section number varies with the temperature threshold value, and more accurate model can be obtained if the value decreases.

Finally, the average temperatures in all sections are calculated, shown as T_{av1}, T_{av2}, T_{av3}, T_{av4}, T_{av5} in Fig. 10, which will be used in step 3.

3) Step 3: The values of resistors and inductors of all Π sections in Fig. 9 are corrected using (9) by the updated average temperatures obtained in step 2.

The circuit model of LTC considering practical frequency and temperature-dependent characteristics has been established based on the aforementioned three steps. Simulation will be performed in Section IV.

IV. Simulation Verification

To validate correctness of the frequency and temperature-dependent RLC circuit model, the simulation in Matlab/Simulink is performed. The advanced frequency-dependent WideBand Line model is provided by OPAL-RT ARTEMiS-SSN library, and it can be easily integrated into Matlab/Simulink model for time-domain simulation [22], where comparative analysis of original WideBand Line model, frequency-dependent RLC circuit model and non-frequency-dependent RLC circuit model is performed. Based on this, the impact of longitude temperature variation on system stability is analysed. The electrical and control parameters of the GCI

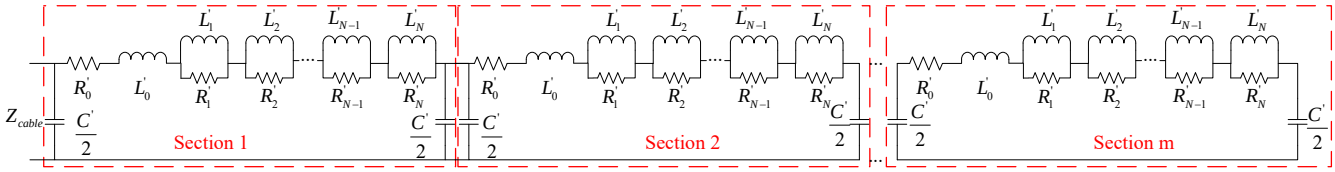

Fig. 9. Multi-segment lumped-parameter RLC circuit model of LTC.

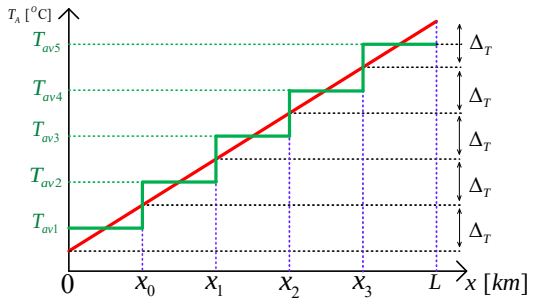

Fig. 10. Linear temperature variation profile along the LTC.

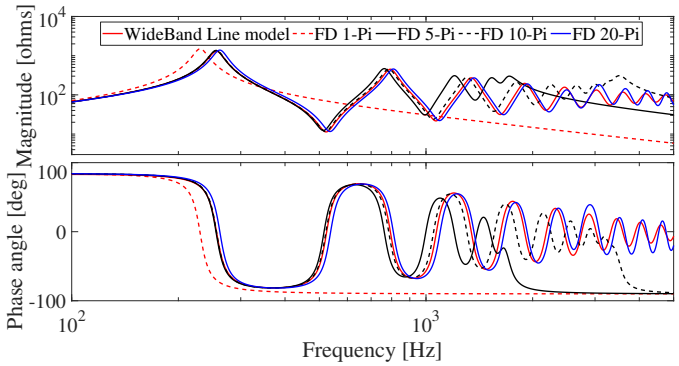

Fig. 11. Terminal impedances of WideBand Line model and RLC circuit models for 40km LTC (FD:Frequency dependent).

simulation model is shown in Table I, and the p.u.l. electrical parameters of the LTC simulation model is shown in Fig. 5.

TABLE I. SYSTEM PARAMETERS OF THE EXEMPLIFIED GCI.

Parameter	Value
dc-link voltage V_{dc}	800V
Grid fundamental frequency	50Hz
Inverter side filter inductor L_{f1}	$1mH$
Grid side filter inductor L_{f2}	$1mH$
Filter capacitor C_f	$4\mu F$
Switching frequency f_s	10kHz
Sampling frequency f_{samp}	10kHz
Grid voltage (phase-to-phase) V_g	380V
Proportional gain of current controller K_p	30
Integral gain of current controller K_i	2000
Proportional gain of PLL K_p	0.7
Integral gain of PLL K_i	3.2
Current reference value i^*_{invd}	30A
Current reference value i^*_{invq}	0

A. *Verification of frequency-dependent RLC circuit model*

Fig. 11 shows the terminal impedances of WideBand Line model, the frequency-dependent RLC circuit with different number of Π sections (1, 5, 10 and 20) for a 40km LTC. It can be seen that fitting accuracy become higher as increase of the number of cascaded Π sections in frequency-dependent circuit model. On the other hand, Fig. 12 shows the terminal impedances of WideBand Line model, the frequency-dependent RLC circuit with 20 Π sections and the non-frequency-dependent RLC circuit model with 20 Π sections for the same 40km LTC. It can be seen that the non-frequency-dependent circuit model has a poorer approximation. The frequency-dependent circuit model with 20 Π sections and the non-frequency-dependent circuit model with 20 Π sections will be used to verify the impact of different models on small-signal stability analysis conclusion.

The equivalent grid impedance Z_{g_cl} is the combination of Z_{Cf}, $Z_{L_{f2}}$ and Z_{LTC}, shown as in Fig. 3. The Bode plots of the equivalent grid impedance using the frequency-dependent circuit model with 20 Π sections Z_{g_cl1}, using the non-frequency-dependent circuit model with 20 Π sections Z_{g_cl2} and using the WideBand Line model Z_{g_cl3} can be calculated from Fig. 12, as shown in Fig. 13. And the terminal impedance of GCI with $f_s = 10$kHz is also plotted. It can be seen that Z_{g_cl1} can approximate Z_{g_cl3} well up to the upper limitation 5kHz of the non-passivity area. However, the non-frequency-dependent circuit cannot reproduce the inherent damping characteristics of LTC. It's clear that there are 7 impedance interaction points between non-frequency-dependent cable model and GCI, of which the phase differences are all larger than 180°. It means that the GCI-LTC system tends to oscillate at multiple frequencies. However, the conclusion that the system tends to be stable will be obtained if WideBand Line model and frequency-dependent model are adopted.

Fig. 14 shows time-domain grid current waveforms and corresponding frequency spectrum when non-frequency-dependent circuit model of 40km LTC is used. It can be seen that there are multiple oscillation frequencies, among which the magnitude of 2562Hz frequency component is largest, since the frequency is located at the non-passivity region [10kHz/6,10kHz/2] and its phase margin is smallest, shown as in Fig. 13. By reducing sampling frequency f_s from 10kHz to 4kHz, the time-domain grid phase currents and frequency spectrum are shown in Fig. 15. Compared with Fig. 14, the dominant oscillation frequency reduces from 2562Hz to

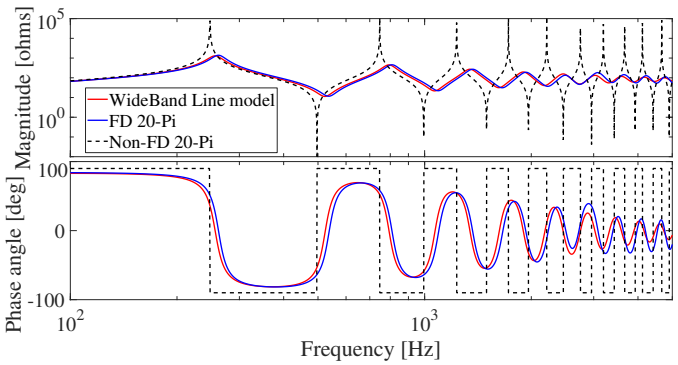

Fig. 12. Terminal impedances of WideBand Line model and RLC circuit models for 40km LTC (FD:Frequency dependent).

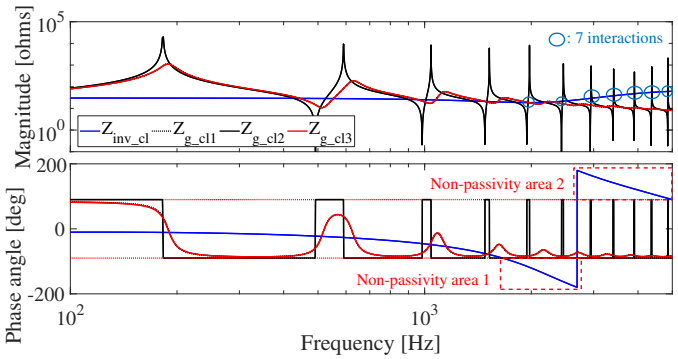

Fig. 13. Bode diagrams of terminal impedances of GCI Z_{inv_cl} with f_s = 10kHz and equivalent grid impedances using different circuit models.

1870 Hz (located in [4kHz/6, 4kHz/2]). It means that the sampling frequency f_s can influence the phase margin of the interaction points, and thus influence which oscillation frequency is dominant.

Similarly, the time-domain grid phase current waveforms and frequency spectrum using WideBand Line model and frequency-dependent circuit model are shown in Fig. 16. It can be seen that grid phase currents are stable and no divergence of grid phase current is observed.

It can be concluded that using the non-frequency-dependent LTC circuit model for stability analysis tends to lead to inaccurate conclusions, due to the lack of representation of inherent damping characteristics.

B. Impact of LTC length on stability analysis

To analyze the impact of LTC length on stability analysis, LTC length is reduced from 40km to 0.5km with sampling frequency f_s = 10kHz. The Nyquist plot of the MLG is shown in Fig. 17(a). It can bee seen that, different from Fig. 17(a), the Nyquist plot encircles (-1, j0) point two times, indicating the system is unstable. Fig. 17(e),(f) shows corresponding time-domain grid phase current waveforms and frequency spectrum. It can be seen that the dominant frequency component appears at 3078Hz, which is located in the non-passivity region of GCI output impedance [10kHz/6, 10kHz/2]. It can be seen that the stability analysis results are different for the same type of LTCs in different lengths.

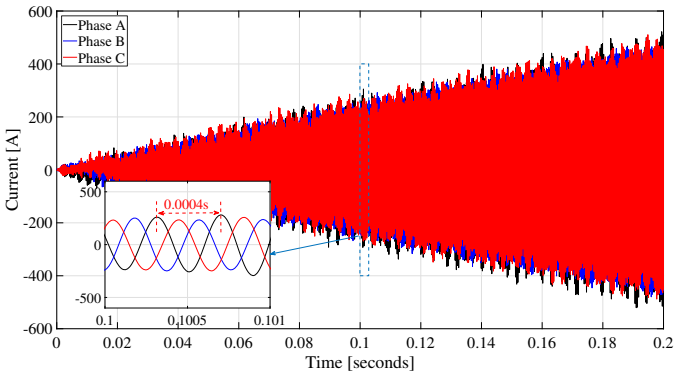

(a)

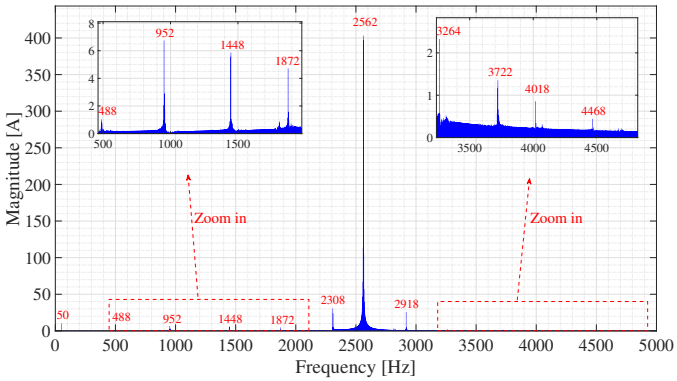

(b)

Fig. 14. Time-domain waveforms and frequency spectrum of grid currents using non-frequency-dependent circuit model for 40km LTC with f_s = 10kHz. (a) Time-domain waveforms; (b) Frequency spectrum.

C. Impact of longitude temperature variation on stability analysis

To further investigate effect of longitude temperature variation on system stability, temperature-dependent circuit model is developed, where electrical parameters of circuit model are revised according to temperature characteristics shown in Fig. 5. The terminal impedances of these frequency-dependent circuit models at different uniformly-distributed temperatures are plotted in Fig. 18. It's clear that the impedance curve shifts leftwards in higher temperature and shifts rightwards in lower temperature.

As an example, time-domain current waveforms and frequency spectrum when the longitude temperature is -50 °C are shown in Fig. 19. Compared with Fig. 17 (b), (c), the dominant oscillation frequency moves rightwards from 3078Hz to 3240 Hz, which results from the rightward shift of the impedance curves interaction points between GCI and LTC at lower temperature. It can be understood that ambient temperature variation may affect system oscillation phenomenon. Thus, temperature-dependent characteristics is important for stability analysis of GCI with LTC.

V. Conclusions

This paper presents a frequency and temperature-dependent circuit model of LTC for small signal stability analysis, where

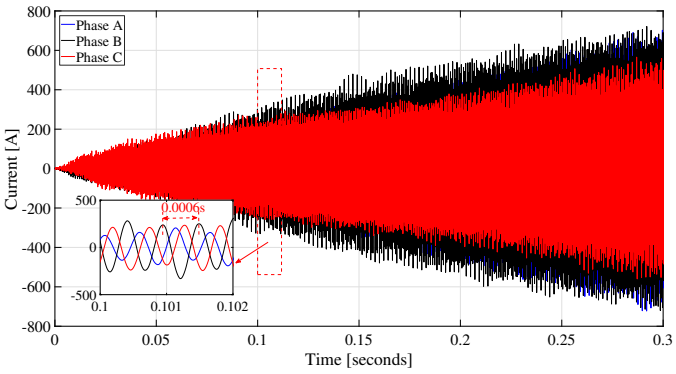

(a)

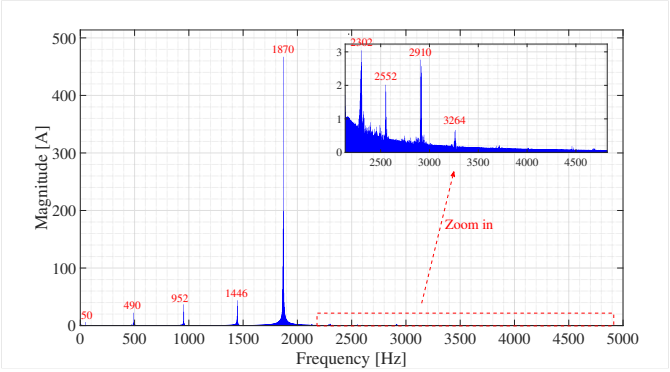

(b)

Fig. 15. Time-domain waveforms and frequency spectrum of grid currents using non-frequency-dependent circuit model for 40km LTC with $f_s = 4$kHz. (a) Time-domain waveforms; (b) Frequency spectrum.

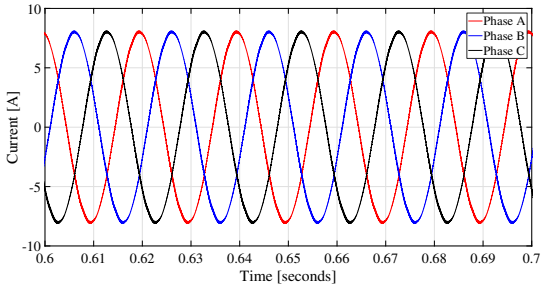

(a)

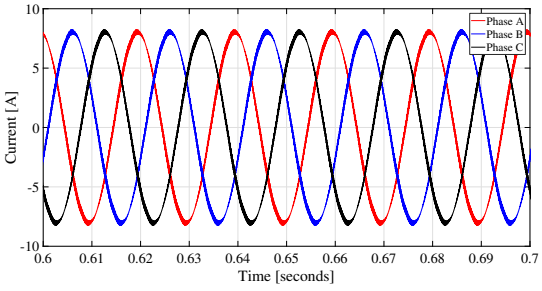

(b)

Fig. 16. Time-domain waveforms of grid currents using WideBand Line model and frequency-dependent circuit model for 40km LTC with $f_s = 10$kHz. (a) WideBand Line model; (b) Frequency-dependent model.

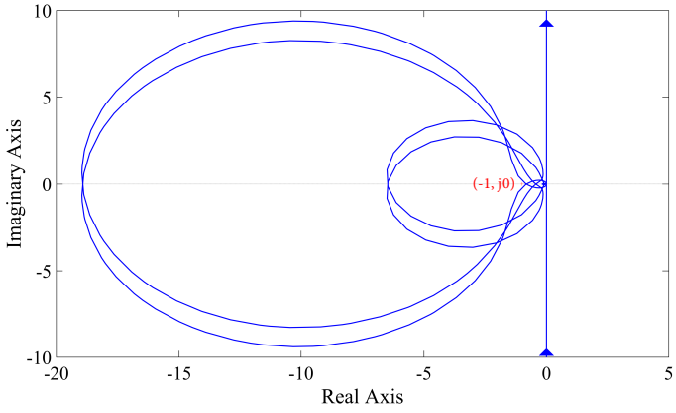

(a)

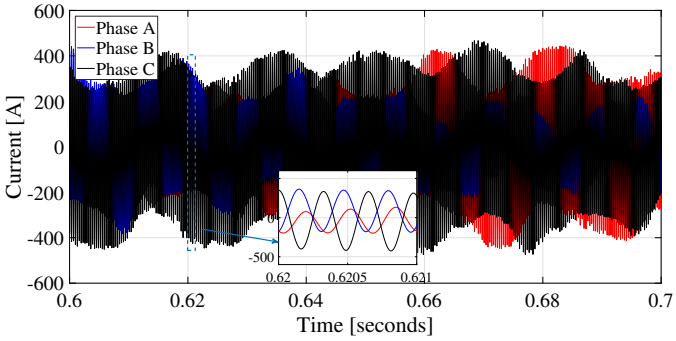

(b)

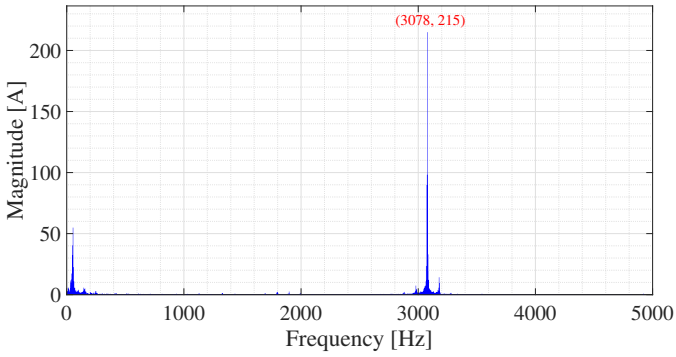

(c)

Fig. 17. Simulation results using frequency-dependent circuit model for 0.5km LTC with $f_s = 10$kHz. (a) Nyquist plot of the MLG; (b) Time-domain waveforms; (c) Frequency spectrum.

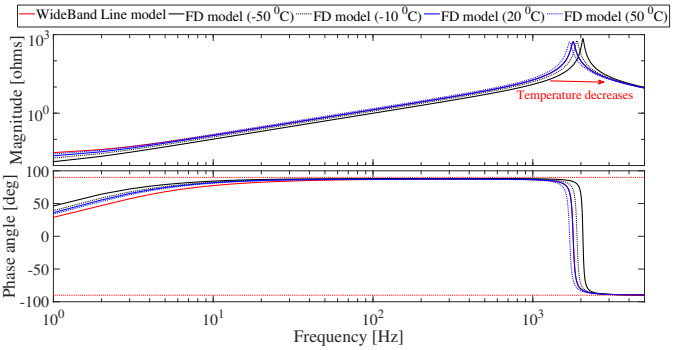

Fig. 18. Terminal impedances of frequency-dependent circuit models for the 0.5km LTC at different temperatures.

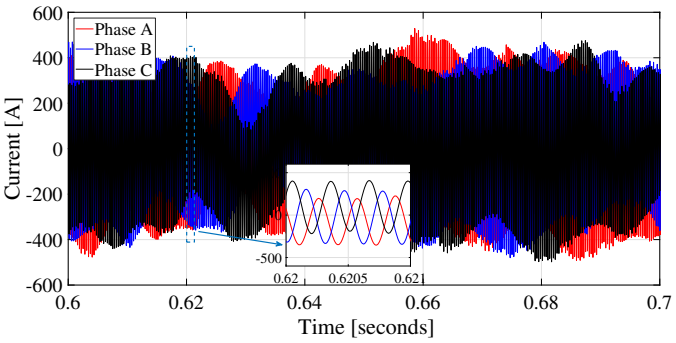

(a)

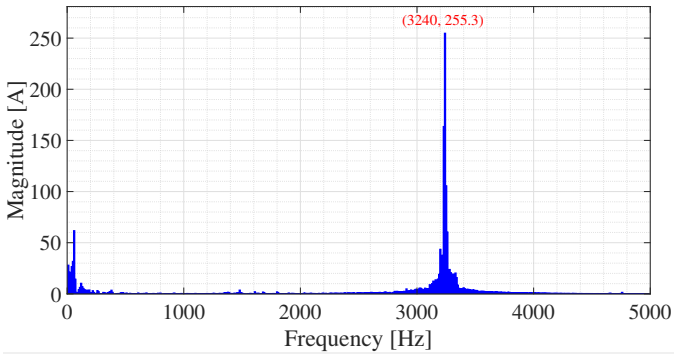

(b)

Fig. 19. Time-domain waveforms and frequency spectrum of grid currents using frequency-dependent circuit model for 0.5km LTC at -50 °C. (a) Time-domain waveforms; (b) Frequency spectrum.

the detailed implementation procedure of modelling is given. P.u.l. impedance of power cable is first obtained by Vector Fitting (VF) algorithm. Then, cascaded-Π circuit model is established to represent terminal impedance of LTC. Finally, the electrical parameters of each Π section are adjusted to according to temperature variation and temperature-dependent model of power cable is formulated. Comparative analysis among WideBand Line model, frequency-dependent model and non-frequency-dependent model is performed. Simulation results show that, the proposed frequency-dependent RLC circuit model can reveal practical damping characteristics of LTC. In addition, electrical parameters of LTC may be perturbed due to variation of longitude temperature. The temperature-dependent characteristics of LTC has to be considered for more accurate small-signal stability analysis of GCI with LTC.

REFERENCES

[1] Z. Chen, J. M. Guerrero, and F. Blaabjerg, "A review of the state of the art of power electronics for wind turbines," *IEEE Trans. Power Electron.*, vol. 24, no. 8, pp. 1859–1875, Aug. 2009.

[2] N. Flourentzou, V. G. Agelidis, and G. D. Demetriades, "VSC-based HVDC power transmission systems: An overview," *IEEE Trans. Power Electron.*, vol. 24, no. 3, pp. 592–602, Mar. 2009.

[3] W. Zhou, Y. Wang, and Z. Chen, "Reduced-order modelling method of grid-connected inverter with long transmission cable," in *Proc. 2018 IEEE 44th IEEE Annual Conference on Industrial Electronics Society*, pp. 1–7.

[4] ——, "Decoupled multi-port impedance modelling method of transmission network in inverter-fed power plant," in *Proc. 2018 IEEE 6th International Conference On Smart Grid (icSmartGrid)*, pp. 129–135.

[5] S. Zhang, S. Jiang, X. Lu, B. Ge, and F. Z. Peng, "Resonance issues and damping techniques for grid-connected inverters with long transmission cable," *IEEE Trans. Power Electron.*, vol. 29, no. 1, pp. 110–120, Jan. 2014.

[6] J. Sun, "Impedance-based stability criterion for grid-connected inverters," *IEEE Trans. Power Electron.*, vol. 26, no. 11, pp. 3075–3078, Nov. 2011.

[7] X. Wang, F. Blaabjerg, and P. C. Loh, "Proportional derivative based stabilizing control of paralleled grid converters with cables in renwable power plants," in *Proc. 2014 IEEE Energy Convers. Congr. and Expo.*, pp. 4917–4924.

[8] X. Zhang, H. S.-h. Chung, L. L. Cao, J. P. W. Chow, and W. Wu, "Impedance-based stability criterion for multiple offshore inverters connected in parallel with long cables," in *Proc. 2017 IEEE Energy Convers. Congr. and Expo.*, pp. 3383–3389.

[9] Y. Song, E. Ebrahimzadeh, and F. Blaabjerg, "Sensitivity analysis of the wind farm high frequency resonance under transmission cable resistance variation," in *Proc. 2018 IEEE Appl. Power Electron. Conf. Expo. (APEC)*, pp. 3218–3224.

[10] J. Beerten, S. D'Arco, and J. A. Suul, "Frequency-dependent cable modelling for small-signal stability analysis of VSC-HVDC systems," *IET Gen., Transm. Distrib.*, vol. 10, no. 6, pp. 1370–1381, May 2016.

[11] S. D'Arco, J. A. Suul, and J. Beerten, "Analysis of accuracy versus model order for frequency-dependent Pi-model of HVDC cables," in *Proc. 2016 IEEE Control and Modeling for Power Electron. (COMPEL)*, pp. 1–8.

[12] R. G. Barry and R. J. Chorley, *Atmosphere, weather and climate*. Routledge, 2009.

[13] V. Cecchi, A. S. Leger, K. Miu, and C. O. Nwankpa, "Incorporating temperature variations into transmission-line models," *IEEE Trans. Power Del.*, vol. 26, no. 4, pp. 2189–2196, Oct. 2011.

[14] M. Bockarjova and G. Andersson, "Transmission line conductor temperature impact on state estimation accuracy," in *IEEE Lausanne Power Tech*, 2007, pp. 701–706.

[15] V. Cecchi, M. Knudson, and K. Miu, "System impacts of temperature-dependent transmission line models," *IEEE Trans. Power Del.*, vol. 28, no. 4, pp. 2300–2308, Oct. 2013.

[16] C. Rakpenthai and S. Uatrongjit, "Power system state and transmission line conductor temperature estimation," *IEEE Trans. Power Syst.*, vol. 32, no. 3, pp. 1818–1827, May 2017.

[17] Y. Wang, X. Wang, F. Blaabjerg, and Z. Chen, "Harmonic instability assessment using state-space modeling and participation analysis in inverter-fed power systems," *IEEE Trans. Ind. Electron.*, vol. 64, no. 1, pp. 806–816, Jan. 2017.

[18] Z. Xin, X. Wang, P. C. Loh, and F. Blaabjerg, "Grid-current-feedback control for LCL-filtered grid converters with enhanced stability," *IEEE Trans. Power Electron.*, vol. 32, no. 4, pp. 3216–3228, Apr. 2017.

[19] S. Buso and P. Mattavelli, *Digital control in power electronics*. Morgan & Claypool Publishers, 2006.

[20] C. R. Paul, *Analysis of multiconductor transmission lines*. John Wiley & Sons, 2008.

[21] B. Gustavsen and A. Semlyen, "Rational approximation of frequency domain responses by vector fitting," *IEEE Trans. Power Del.*, vol. 14, no. 3, pp. 1052–1061, Jul. 1999.

[22] C. Dufour, H. Saad, J. Mahseredjian, and J. Bélanger, "Custom-coded models in the state space nodal solver of artemis," in *Proc. Int. Conf. Power Syst.Trans. (IPST-2013)*, 2013.